Measurements and modeling of CO 4th positive (A -X) radiation

Sean Mcguire, Augustin Tibère-Inglesse, Pierre Mariotto, Brett A Cruden, Christophe O. Laux

Measurements and modeling of CO 4th positive (A - X) radiation

Sean D. McGuire[a,1,*], Augustin C. Tibère-Inglesse[a,2], Pierre B. Mariotto[a,2], Brett A. Cruden[b,3], Christophe O. Laux[a,4]

[a]*Laboratoire EM2C, CNRS UPR288, CentraleSupélec, Université Paris Saclay, 3 rue Joliot-Curie, Gif-sur-Yvette, France*

[b]*AMA Inc. at NASA Ames Research Center, Moffett Field, CA 94035, USA*

Abstract

We present absolute intensity measurements of CO 4th positive emission from a CO_2/Ar plasma jet produced using an atmospheric pressure plasma torch facility. The centerline temperature of the plasma jet is approximately 6300 K. A VUV emission spectroscopy system was adapted to the plasma torch facility to measure spectrally resolved emission down to 140 nm. The emission from the plasma in the VUV, UV and near IR is consistent with thermochemical equilibrium. Carbon lines in the UV and VUV are found to be optically thick and their amplitude is therefore substantially affected by the line broadening parameters used for the calculation. For the CO 4th positive emission, these measurements test the performance of various models for the electronic transition moment function (ETMF). These ETMFs are used to calculate sets of Einstein coefficients that are used by SPECAIR to calculate the spectrally resolved emission of the plasma for comparison with experiments. We find that the EMTF of Kirby and Cooper and Spielfiedel accurately reproduce the measured emission from 150 - 215 nm.

1. Introduction

Radiative heat flux is expected to be an important contributor for manned space missions beyond Earth orbit, due to the large capsule size and high entry velocity associated with such missions.[1, 2, 3, 4] The radiative heat flux is expected to become significant for Mars and Venus entries at speeds above 7.5 km/s. The Pioneer Venus missions entered at velocities in excess of 11 km/s. For Mars entry scenarios, Johnston, Brandis and Sutton [5] provide simulated values of the convective and radiative heat fluxes for the Mars Pathfinder and hypersonic inflatable aerodynamic decelerator (HIAD) missions. They provide estimates of the radiative heat flux that fall between 25 - 37 % of the total heat flux for the HIAD mission. Beyond direct entry scenarios, there is significant interest in using aerocapture maneuvers for missions to Mars and Venus in order to increase the percentage of useful payload.[6, 7, 8, 3] Depending upon the specific parameters of this maneuver, the radiative heat flux can represent an important portion of the total heat flux. For Venus

*Corresponding author

Email address: sean.mc-guire@centralesupelec.fr (Sean D. McGuire)

[1]Assistant Professor, Laboratoire EM2C, CNRS, CentraleSupélec

[2]Doctoral Student, Laboratoire EM2C, CNRS, CentraleSupélec, Université Paris Saclay

[3]Senior Research Scientist, Aerothermodynamics Branch, NASA Ames Research Center

[4]Professor, Laboratoire EM2C, CNRS, CentraleSupélec

and Mars atmospheres, composed primarily of CO_2, the CO($A\,^1\Pi \rightarrow X\,^1\Sigma^+$) transition, called the CO fourth positive system and denoted CO(4+), represents either a significant or dominant portion of the radiative heat flux [9, 2]. Cruden, Prabhu and Martinez [2] measured the CO(4+) contribution to be between 54 - 64% of the total radiance from measurements in the electric arc shock tube (EAST) facility for Mars and Venus entry test conditions. It is therefore important to validate the radiation models used for this system and to reduce the corresponding uncertainty. Accurate values of the Einstein coefficients are also necessary to correctly scale the rates of CO recombination.[5, 10, 11, 12, 13]

In 2013, researchers at NASA Ames studied the radiation of CO(4+) in the EAST facility [9, 2] to characterize the radiative heat flux under Venus and Mars entry conditions. They compared measurements of CO(4+) radiation with predictions made with the HARA [14, 15], HyperRad [16] and NEQAIR [17] radiation codes. When the equilibrium post-shock temperature was used, the models underestimated the measured radiation by a factor of 2. They noted that a large portion of the CO(4+) spectrum was blackbody limited. Fitting a blackbody curve to this portion of the spectrum yielded a second estimate of temperature, found to be 2 - 9 % higher than the equilibrium shock calculation. By using this second temperature, they achieved better agreement between the radiation models and the measurements, yet discrepancies remained at certain wavelengths. The purpose of this work is to evaluate and validate the radiative models for CO(4+) emission. The plasma torch facility at laboratoire EM2C operates at atmospheric pressure and provides a plasma in chemical and thermal equilibrium. This enables more definitive tests of the radiation models because the population distribution and concentration of the emitting species are accurately known. Specifically, this paper compares the performance of five CO(4+) radiation models against the experimental data obtained in the VUV and identifies which models work best. The transition probabilities tested here are based on the electronic transition moment functions of DeLeon [18, 19], Kirby and Cooper [20], Spielfiedel et al [21], Chantranupong et al [22] and Cheng et al [23].

2. Radiation transition probabilities of CO(4+)

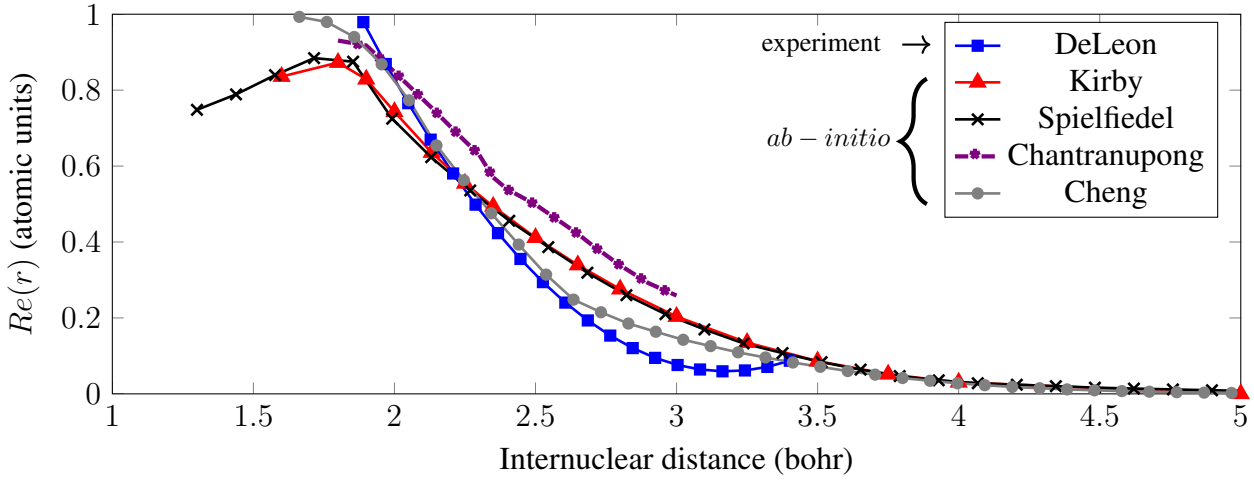

Figure 1: Electronic transition moment function ($Re(r)$) taken from DeLeon [18, 19], Kirby and Cooper [20], Spielfiedel et al [21], Chantranupong et al [22] and Cheng et al [23]

For the analysis presented here, all experimental results are compared with simulations obtained using SPECAIR.[24, 25, 26] The spectral positions of the CO(4+) lines are calculated with the Dunham expansion coefficients of Farrenq et al [27] and Simmons et al [28]. Transitions between levels $\nu' = 0, 23$ of the excited state and $\nu'' = 0, 41$ of the ground state are included in the calculation. The Einstein coefficients for each rovibrational transition are calculated using the method outlined in Laux and Kruger [29]:

$$A_{\nu'\nu''} = \frac{64\pi^4\nu^3}{3hc^3} \frac{(2 - \delta_{0,\Lambda'+\Lambda''})}{(2 - \delta_{0,\Lambda'})} Re^2_{\nu'\nu''} \tag{1}$$

where:

$$Re^2_{\nu'\nu''} = \left[\int_0^\infty \psi_{\nu'}(r)\, Re(r)\, \psi_{\nu''}(r) dr\right]^2 \tag{2}$$

$Re_{\nu'\nu''}$ is the electronic-vibrational transition moment, $\psi_{\nu'}$ and $\psi_{\nu''}$ represent the vibrational wavefunctions of the upper and lower states respectively, Λ' and Λ'' represent the projection of the orbital angular momentum of the upper and lower states respectively and δ is the Kronecker delta function. The above expressions are taken from Schadee [30]. Additional relations are contained in Appendix C.

For these calculations, the Rydberg-Klein-Rees (RKR) method was first used to determine the potential energy curves for the X and A states of CO. The vibrational wavefunctions were then calculated. Finally, the electronic transition moment $Re(r)$ was taken from one of five datasets reported in the literature: DeLeon [18, 19], Kirby and Cooper [20], Spielfiedel et al [21], Chantranupong et al [22] and Cheng et al [23]. DeLeon supplies an interpolation based on his experimental data and those previously reported by Field et al [31]. The ETMF of Kirby and Cooper [20], Chantranupong et al [22], Cheng et al [23] and Spielfiedel et al [21] are *ab initio* calculations. Figure 1 shows a comparison of the electronic transition moments. To comply with the convention outlined by Whiting [32], the data of Kirby and Cooper have been divided by a factor of $\sqrt{2}$. The *ab initio* calculations of Kirby and Spielfiedel are close - to within 5%. In the sections that follow, we will therefore use the ETMF of Kirby and Cooper for the calculations and treat these ETMFs as identical.

Appendix A shows some of the most important vibrational bands present in the spectrum for the conditions studied. Figure 2 shows the band origin wavelengths associated with each r-centroid for the observed transitions. All r-centroids fall between 2 and 3 bohr. In looking at Fig. 1, we note that this is where there is a large discrepancy between the various models for $Re(r)$. Note we do not use the r-centroid approximation in the calculation of the Einstein coefficients. However, this approximation proves useful in visualizing where on the $Re(r)$ curve the vibrational bands are located. Finally, Appendix B includes a discussion of line broadening for the modeling of optically thick atomic lines in the VUV/UV portions of the spectrum.

3. Experiment

3.1. Plasma torch facility

The plasma torch facility is a TAFA Model 66 inductively coupled plasma (ICP) torch powered by a 120 kVA radio frequency LEPEL Model T-50-3 power supply. The power supply operates at

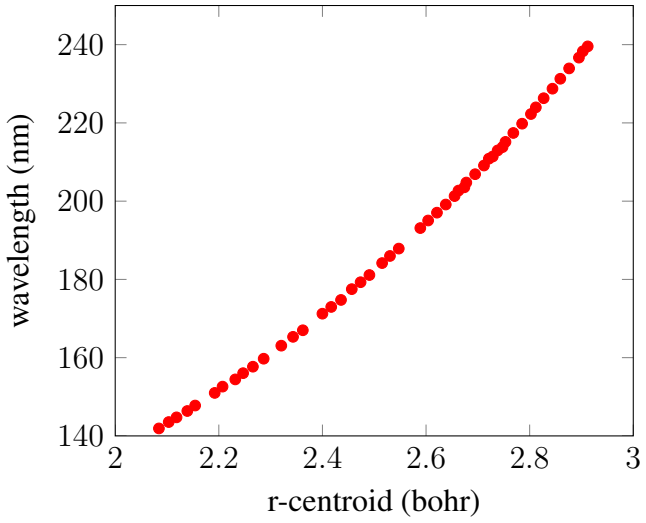

Figure 2: Band origin wavelength versus r-centroid for the observed bands (see Fig. A.16).

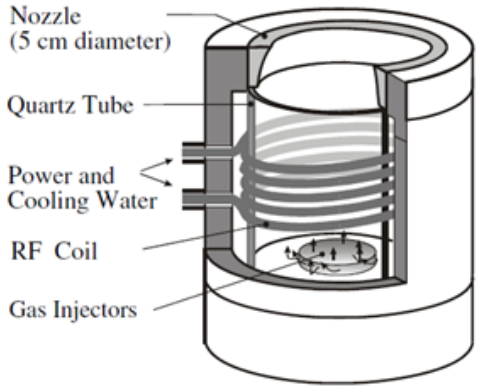

Figure 3: Plasma torch head and nozzle assembly. The gas injectors include radial, swirl and axial injectors.

4 MHz and provides a maximum of 12 kV DC and 7.5 A to the oscillator plates. Details of the plasma torch facility are provided in previous publications [24, 33]. For the experiments presented here, a 5-cm diameter exit nozzle was used. The plasma at the exit of the torch is at atmospheric pressure. Figure 3 shows a schematic of the facility. Radial, swirl and axial gas injectors can be used for gas injection. Calibrated flow meters from Bronkhorst (F-202AV, F-201AC, F-201CV) are used to control the mass flow rate of each gas through the system.

A significant effort was invested in determining a suitable mixture and injection procedure for introducing the flow into the torch in order to obtain an axisymmetric plasma with a smooth temperature profile. This torch has been previously operated with either air or mixtures containing comparatively small quantities of argon. For such mixtures, smooth and axisymmetric temperature profiles are quite easily obtained and are not sensitive to the method of injection - i.e. the relative values of radial, swirl and axial injection. In the present experiments, argon was the predominant species. In many cases, the temperature profiles obtained with an argon rich mixture were experimentally observed to be asymmetric about the centerline axis. However, a symmetric profile was necessary for the Abel inversion used in the calculation of the temperature profile. To ensure that

the profile was axisymmetric, we found that increasing the swirl helped and chose the relative level of radial and swirl axial injection accordingly. Axisymmetry was checked by comparing left/right half profiles. The large majority of the mixture injected ($\sim 91\%$) passed via the radial and swirl injectors and was premixed. As a percentage of the total flow rate, approximately 54% was injected via the radial injector and 37% via the swirl injector. A small amount of axial injection ($\sim 10\%$) of pure argon was also used. This small amount of argon axial injection was found to enhance the plasma stability during operation. The reported value of 3.79 g/s argon injected includes this axial component.

The torch could not be operated with large quantities of CO_2 as it could not sustain the level of ionization necessary for preserving the plasma. Argon is comparatively easy to ionize and its emission does not significantly interfere with the emission from the CO(4+) band in the plasma. It is included in the SPECAIR calculations to account for any argon lines that appear in the spectra. For the results presented in this paper, 3.79 g/s of Ar ($\geq 99.99\%$ purity) and 0.352 g/s of CO_2 ($\geq 99.9\%$ purity) were injected into the torch. The uncertainties on these mass flow rates are both on the order of $\pm$ 2 %. This combination provided a stable plasma with a relatively hot centerline temperature.

Temperature measurements were obtained from the absolute intensity of emission lines of atomic carbon (833 nm), oxygen (777 nm) and argon (764 nm). These measurements were made using a UV-VIS spectrometer (Acton SpectraPro 500i), intensified PI-MAX camera and imaging setup. A longpass filter was installed in the optical path to suppress higher order diffraction interferences. The imaging system is comprised of two parabolic mirrors and a periscope to image the spectrometer slit across the jet profile. Intensity measurements are Abel-inverted to provide spatially resolved intensity measurements. The procedure for these emission-based temperature measurements is documented in Refs. [24, 34]. The analysis relies upon the assumption of thermochemical equilibrium and rotational symmetry of the plasma jet. It also assumes that the atomic emission used for the temperature analysis is optically thin.

3.2. VUV spectrometer

The spectrometer and imaging system used for VUV measurements are shown in Figure 4a. The spectrometer is a McPherson VUV spectrometer (Model 218). An imaging box made of steel is attached to the spectrometer. Two spherical mirrors of 50 cm focal length inserted into this box are used to image the slit onto the torch - the spectrometer slit and torch are located at the focus of each mirror and therefore there is no image magnification. These mirrors are coated with the Acton Optics #1200 coating for 120 nm. The VUV system provides line-of-sight measurements along the chord intersecting the plasma centerline, 2.5 cm downstream of the nozzle exit.

For comparing measurements with SPECAIR calculations, the radiative transport equation is solved along the line-of-sight using the temperature profile measured using the UV-VIS spectrometer. Figure 11 shows the slit function of the VUV system for the CO(4+) measurements below 300 nm.

An overview of the VUV emission system is shown in Fig. 4a. The optical layout for the VUV system is shown in Fig. 4b. Through the use of a rotary vane roughing pump and a turbopump (80 liters/sec), the system was pumped down to a pressure of approximately 5.0×10^{-5} Torr for all tests. The rotary vane pump was equipped with a zeolite adsorbent filter to prevent oil backstreaming into the optical system. An argon purge (AirLiquide, Argon Alphagaz 2, $\geq 99.9999\%$ pure) was used to remove oxygen from the final 10 cm of the optical path that is not under vacuum. A MgF_2 window

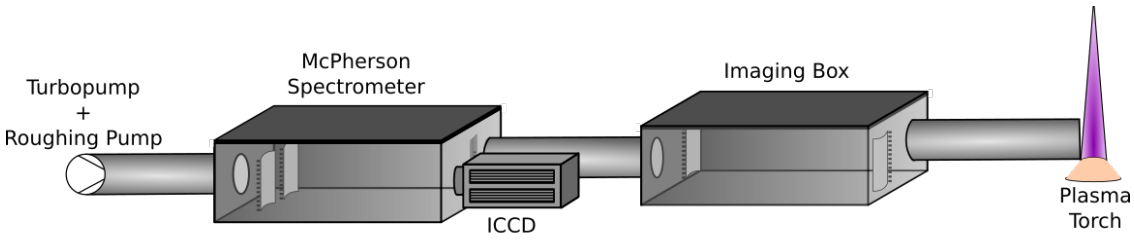

(a) VUV spectrometer and imaging system used for measurements of CO(4+).

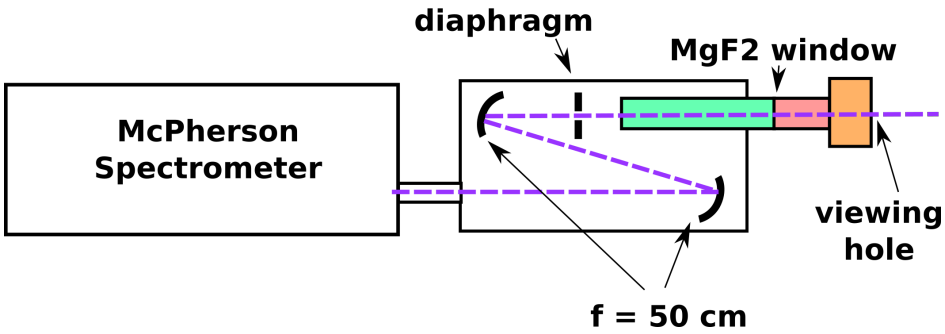

(b) Optical layout of the VUV system showing the mirrors, diaphragm, adapting tube and their relative locations with respect to the spectrometer. The adapting tube is color-coded as in Fig. 4c to illustrate where the various components fall. The optical path is indicated by the dashed violet line.

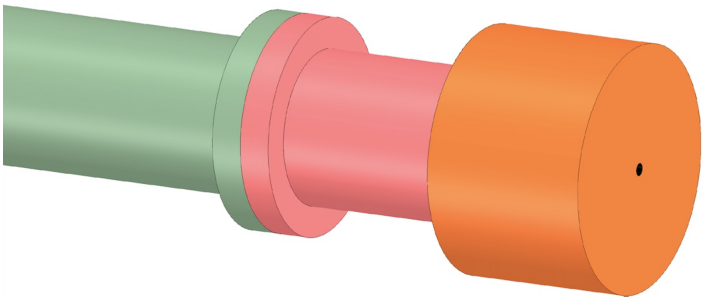

(c) Diagram showing the final tube protruding from the imaging box and coming into contact with the plasma.

Figure 4

separated this argon purged section from the primary section under vacuum. A diagram of this final 10 cm section is shown in Fig. 4c. The portion in green is under vacuum and was manufactured out of PEEK, a vacuum compatible material. The portions in red and orange are under an argon purge. The portion highlighted in orange is water-cooled copper, whereas the portion highlighed in red is manufactured out of Teflon. The materials PEEK and Teflon were chosen in order to provide electrical isolation from the torch head which rests at 10 kV. A continuous argon purge was run at a pressure slightly above 1 atm to prevent oxygen from leaking into the system. Pressure relief ports were drilled in the red teflon piece to permit a portion of the argon flush to exit via these holes, rather than entirely into the plasma. The remaining portion exited through the final viewing hole, directly entering the plasma jet. Tests were conducted to verify that this purge did not affect the measured radiation (section 4.2). The final viewing hole in the water-cooled copper piece is 2

mm in diameter. The optical system was focused in the center of the plasma jet, 2.5 cm from the copper surface.

For calibration in absolute intensity an Optronics OL550 Tungsten ribbon lamp was used for wavelengths above 400 nm. An argon mini-arc discharge, with calibration traceable to NIST standards between 120 and 400 nm [35], was used for wavelengths below 400 nm. In order to calibrate the system using the argon discharge, a modification of the VUV system was required. The final 10 cm of the imaging line was replaced with an adaptor to mount the system directly to the discharge housing. The sliding tube protruding from the imaging box and holding this entire assembly was adjusted so that the argon discharge emission was located at the system focus. A diaphragm placed in the imaging box served as the limiting aperture of the system so that the collection solid angle was the same for both the measurements made in the plasma torch and the calibration measurements. For these VUV/UV calibration measurements, we found that the level of stray light was too large to make calibrations below approximately 160 nm. To address this problem, a VUV transmission filter (eSource Optics 50150FBB) with a peak transmission wavelength of 146 nm and bandwidth of 62.5 nm was employed. This significantly cut down on the stray light which was mostly due to emission from the argon discharge in the UV and visible spectral regions. The reported transmissivity of this filter was verified by performing calibrations with and without the filter. For the wavelengths above 160 nm, for which it was possible to compare the two calibrations, the reported filter transmission was found to be accurate. Therefore, this filter was only put in place for the calibration between 140 and 300 nm. It was not installed for measurements of the plasma emission as it would have significantly and unnecessarily reduced the available signal.

4. Results

4.1. Temperature measurements

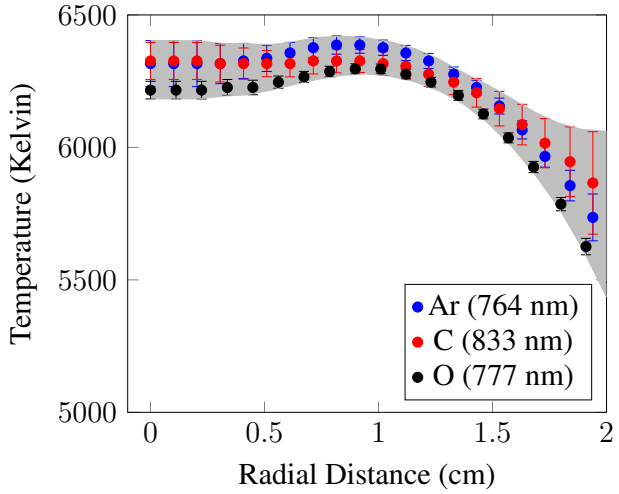

Figure 5: Temperatures obtained by measuring absolute emission from several atomic features. Uncertainty bars are included in the figure. The grey region is bounded by the maximum and minimum temperature profiles based upon the atomic measurements. Note that the water-cooled copper piece is located at a radial distance of 2.5 cm.

Figure 5 shows the temperature measurements for the mixture studied here. The difference in the nominal temperatures between the argon, carbon and oxygen lines is approximately 85 K.

We therefore treat the plasma to be in equilibrium and apply the maximum uncertainty range, highlighted in Fig. 5. This range will be used later in the SPECAIR calculations to determine maximum and minimum emission spectra. Figure 6 shows the chemical composition of the plasma determined with NASA CEA [36] and using the nominal temperature from the argon 764 nm line.

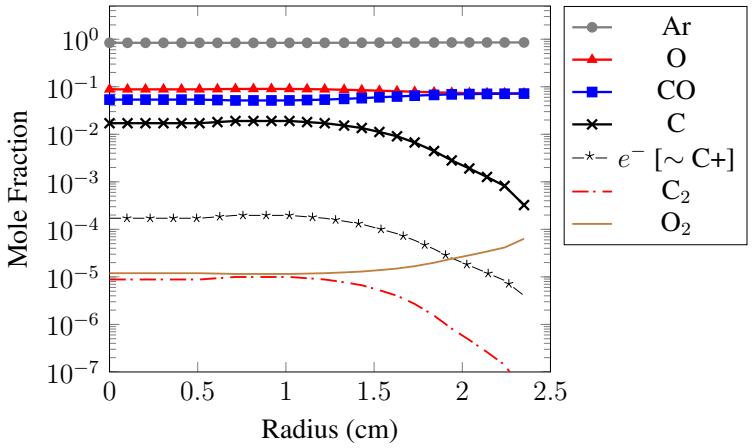

Figure 6: Equilibrium mole fractions as a function of radial distance. The calculations were done using NASA CEA [36] based upon the temperature profile measured using the argon 764 nm line. The electron mole fraction is approximately equal to the C^+ mole fraction.

4.2. Measurements in the UV/VIS spectral regions

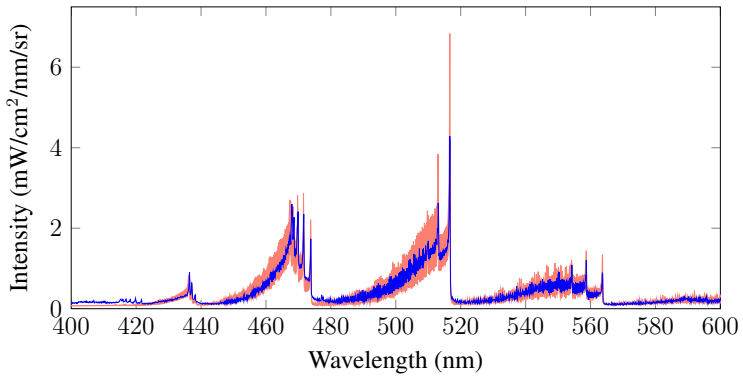

Figure 7: Comparison between measured C_2 Swan emission (blue) and the SPECAIR calculation (red). The SPECAIR calculation is bounded by the maximum and minimum intensities possible given the uncertainties in the temperature measurements. An offset of 0.07 $mW/cm^2/nm/sr$ was added to the SPECAIR spectrum.

As an additional confirmation that the plasma is in thermochemical equilibrium, we measured C_2 $d\,^3\Pi_g - a\,^3\Pi_u$ (Swan system) emission using the UV/VIS spectrometer setup. A grating of 600 grooves/mm blazed at 300 nm was used and the slit function had a FWHM of approximately 0.2 nm. A long pass filter ($\lambda > 350\,nm$) was also used to suppress higher order interferences within the spectrometer. These measurements were compared with SPECAIR predictions based upon the measured temperature profiles of Fig. 5. SPECAIR modeling of C_2 Swan radiation has been previously validated by Caillault et al.[37] An offset of 0.07 $mW/cm^2/nm/sr$ was added

to the SPECAIR spectrum to compensate for a small continuum that is not modeled. The mole fraction of C_2 is on the order of $5 - 10 \times 10^{-6}$ (Figure 6). Figure 7 shows a comparison between the measured and computed spectra. The good agreement is consistent with the plasma being in thermochemical equilibrium.

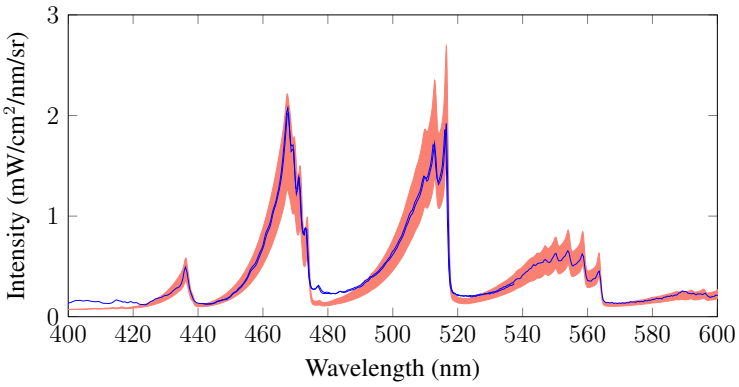

Figure 8: Measurements of the C_2 Swan bands (450 - 650 nm) using the VUV system in its final configuration. The SPECAIR calculation is bounded by the maximum and minimum intensities given the uncertainties in the temperature measurements. Two experimental measurements are included on this plot and overlap between approximately 440 and 520 nm.

To verify that the VUV system did not perturb the central portion of the plasma responsible for the measured emission, measurements were made in the UV/VIS region of the spectrum but using the VUV spectrometer. For these measurements, a low resolution grating of 180 grooves/mm was used. These measurements were compared with SPECAIR calculations that have been shown to reproduce the unperturbed torch signal in Fig. 7. Figure 8 shows the comparison with SPECAIR to be good. Again, a constant background of 0.07 $mW/cm^2/sr/nm$ was added to the SPECAIR calculation to account for continuum radiation not modeled in SPECAIR. Aside from features at 400 nm, believed to be the C_2 Deslandres-d'Azambuja system not modeled in SPECAIR, the good agreement confirms that the presence of the water-cooled copper piece and argon purge adjacent to the plasma are not perturbing the central region of the plasma responsible for the emission.

4.3. VUV measurements

Figure 9 shows a SPECAIR calculation of the CO_2/Ar plasma emission at the exit of the torch with and without self-absorption. The calculation was done by assuming thermochemical equilibrium and by solving the radiative transport equation across the profile defined by the measured temperatures reported in Fig. 5. It is worth noting that the CO(4+) emission becomes heavily optically thick in the VUV below 180 nm. All carbon lines, including the one at 248 nm, are also heavily optically thick. The optically thin and optically thick calculations presented in Fig. 9 differ by several orders of magnitude for the lines below 200 nm, indicating the extent of optical thickness. Figure 10 shows a zoom on the calculated 193 nm carbon line to illustrate the severe impact of self-absorption on the line profile.

For the VUV measurements, a high-resolution 2400 grooves/mm grating was used in the VUV spectrometer. The slit function has an approximate FWHM of 0.08 nm and is shown in Figure 11 for reference. Figures 12a - 12d show the comparison between the measured spectrum and SPECAIR calculations based upon the ETMFs from Kirby [20], Chantranupong [22], Cheng [23]

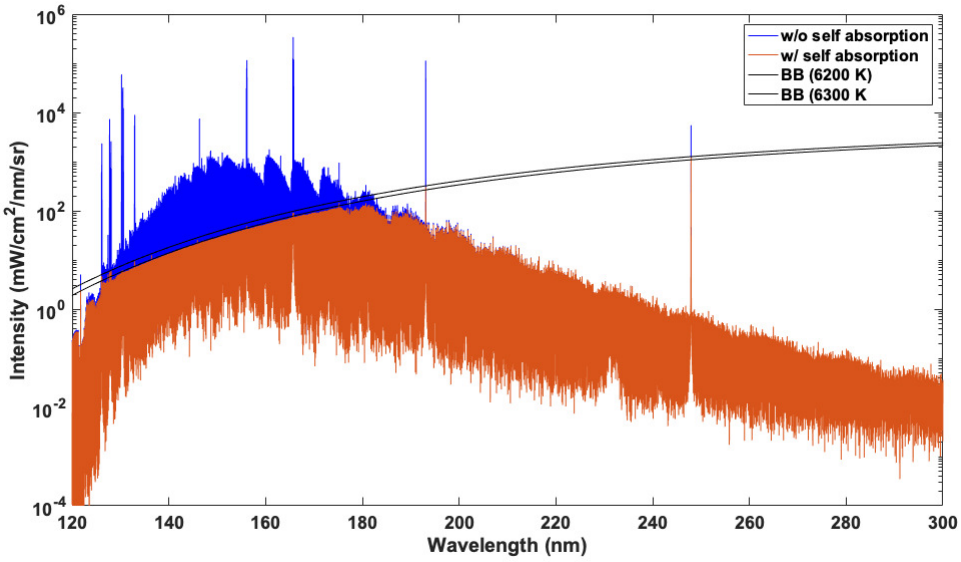

Figure 9: SPECAIR calculation with and without self-absorption to illustrate the optically thick nature of the emission in the VUV. The Kirby electronic transition moment function was used for the calculation of the CO(4+) bands. This calculation was done without a slit function.

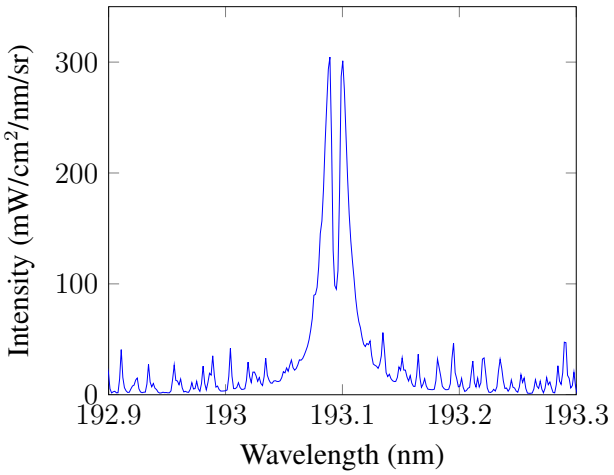

Figure 10: Zoom on the calculated 193 nm C line structure from the calculation in Fig. 9

and DeLeon [18, 19]. Note that the C_2 $D^1\Sigma_u^+ - X^1\Sigma_g^+$ (Mulliken system) is included in SPECAIR calculations and appears at 230 nm. We used the model of Bruna and Wright for this molecular system.[38] For these plots, the uncertainty in the temperature measurements is carried through the SPECAIR calculation. The bounds on the SPECAIR calculation correspond to the minimum and maximum possible temperature based upon the measured temperature profile shown in Fig. 5. The Kirby ETMF agrees within the error bars from between 162 - 210 nm. Chantranupong is on the lower end of the error from 162-175 nm, outside the range from 175-218nm, and in agreement above 218 nm. Cheng agrees well from 162-180 nm, and is too high at longer wavelengths. DeLeon is in agreement only from 162-170nm, and too high everywhere else. These differences stem from the corresponding differences in the ETMF's shown in Fig. 1 for radii between 2 and

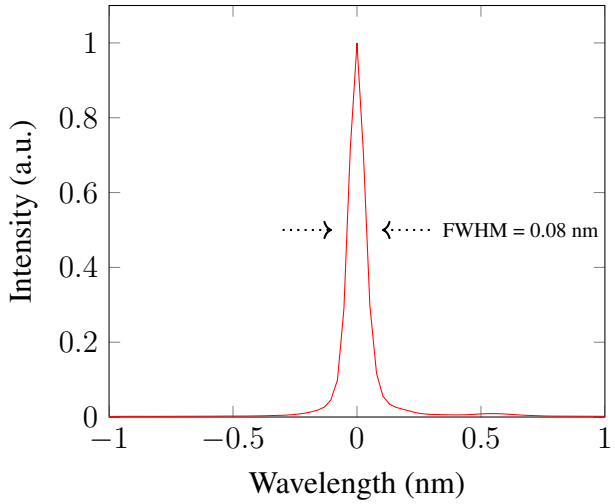

Figure 11: Measured slit function of the VUV system.

3 bohr. Concerning the Kirby ETMF calculations, the discrepancy with the experimental measurements below 162 nm can be accounted for by cold gas absorption in the shear layer. This is discussed below. Sources of radiation that could cause the discrepancy above 210 nm were checked, including O_2 Schumann-Runge from entrained oxygen and carbon bound-free, though neither were strong enough to account for the difference. Thus, the discrepancy above 210 nm may indicate that Kirby's ETMF should be reevaluated at larger separation distances (see Fig. 2) that impact this region of the spectrum.

None of the curves reproduce the spectra accurately below approximately 165 nm. This is attributed to absorption from cold gases in the VUV. CO_2 is present in the shear layer of the jet, where temperatures are cold enough that it remains undissociated. To evaluate the potential impact of CO_2 on the spectra, the cross-sections for cold CO_2 absorption from Thompson, Harteck and Reeves [39] were used. This dataset includes data from Watanabe, Zelikoff and Inn [40]. Given the injection mixture used for these measurements a CO_2 mole fraction of $x_{CO2} \approx 0.078$ is calculated at room temperature. Adding about 0.5 cm of cold gas absorption to the measurement reproduces nicely the experimental data (see Figs. 13a - 13d). This would be consistent with local cooling of the gas mixture near the water-cooled copper piece (Fig. 5). Another possible species for absorption of the signal would be O_2 due to air entrainment around the boundaries of the jet. Adding about 50 μm of cold O_2 absorption also produces the level of absorption needed to match the profile produced by CO_2 absorption. Note that this equivalent path length of O_2 would not be consistent oxygen levels associated with the level of vacuum in the system or the purity of the argon purge. Rather, it would have to come from cold air entrainment into the edges of the jet. The absorption profiles of O_2 and CO_2 are quite similar in shape over the wavelength range 145 - 160 nm and thus produce a similar result using either molecule as the absorber. Therefore, while CO_2 is a likely absorber given that it is known to be present, it is possible that some amount of O_2 is also contributing to the reduced signal at low wavelengths. Based upon the comparison with SPECAIR predictions, the measurements appear to be free from cold gas absorption down to about 165 nm. Table 1 shows how the integral of the measured spectrum, from 165 - 220 nm, compares with the model predictions.

Atomic carbon has several lines that emit in the VUV and UV. Figure 14 shows zooms on the

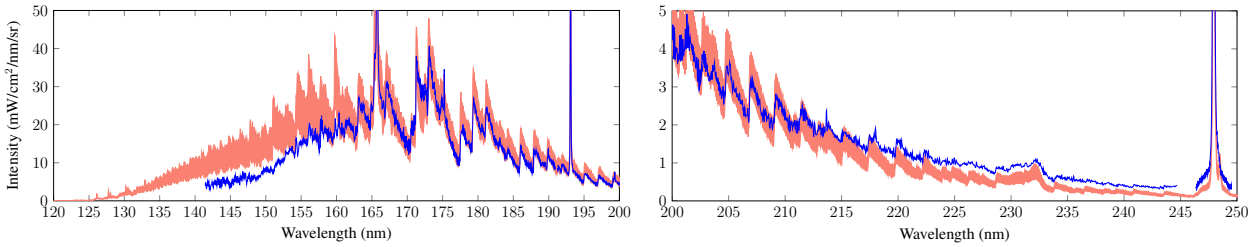

(a) Experiment (blue) and SPECAIR calculations (red) based upon the Kirby electronic transition moment function.

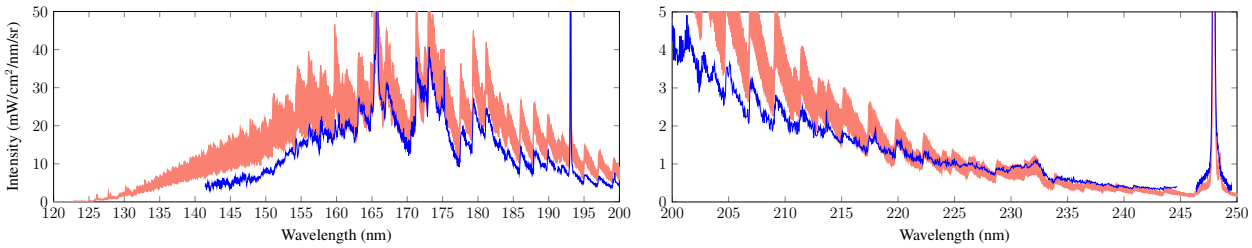

(b) Experiment (blue) and SPECAIR calculations (red) based upon the Chantranupong electronic transition moment function.

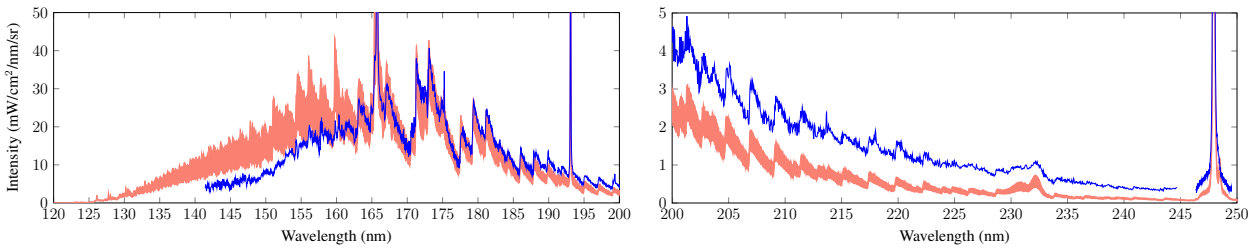

(c) Experiment (blue) and SPECAIR calculations (red) based upon the Cheng electronic transition moment function.

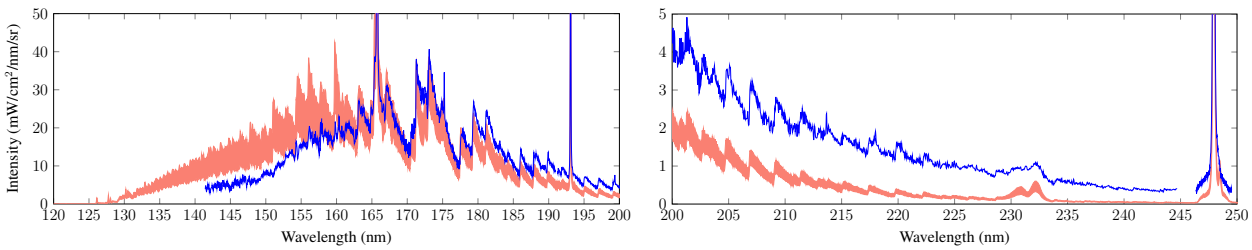

(d) Experiment (blue) and SPECAIR calculations (red) based upon the electronic transition moment functions of DeLeon et al.

Figure 12

193 and 248 nm carbon lines that were not visible in the previous figures. The calculation for the underlying CO bands was done with the Kirby ETMF. The Einstein coefficients for these carbon lines were taken from the NIST atomic spectral database [41] which, in turn, cites Fischer [42] as the source for these coefficients. As discussed in Appendix B, Doppler broadening is the dominant line broadening mechanism. However, for these atomic lines of carbon, van der Waals broadening also plays an important role. The Einstein coefficient accuracy for the 193 nm line is quoted to be within 3%. The Einstein coefficient accuracy for the 248 nm line is quoted to be 18%. Both lines appear to be well captured.

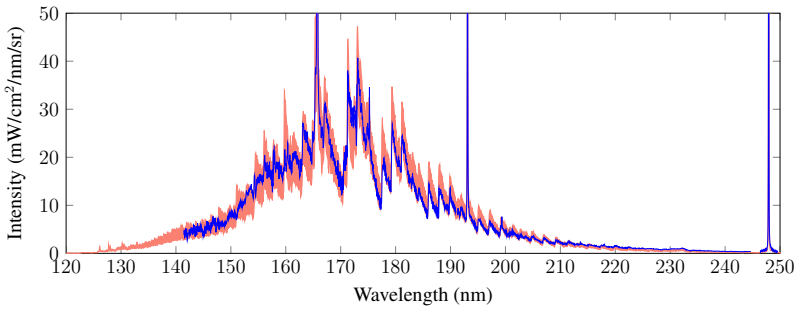

(a) Experiment (blue) and SPECAIR calculations (red) using Kirby electronic transition moment function with a 0.5 cm absorption path length of cold CO_2 ($x_{CO2} = 0.078$).

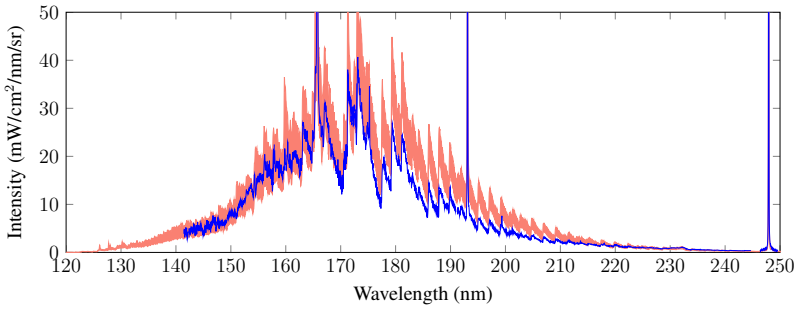

(b) Experiment (blue) and SPECAIR calculations (red) using Chantranupong electronic transition moment function with a 0.5 cm absorption path length of cold CO_2 ($x_{CO2} = 0.078$).

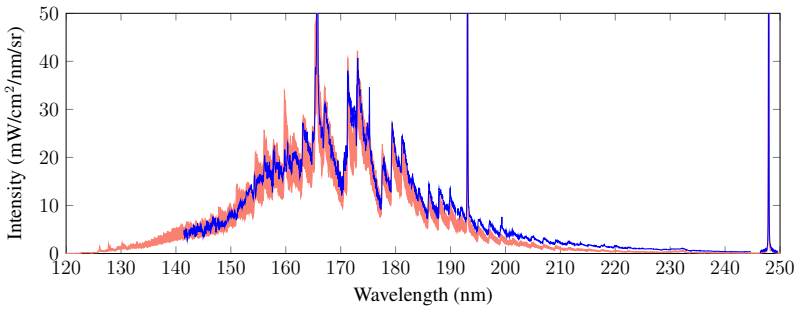

(c) Experiment (blue) and SPECAIR calculations (red) using Cheng electronic transition moment function with a 0.5 cm absorption path length of cold CO_2 ($x_{CO2} = 0.078$).

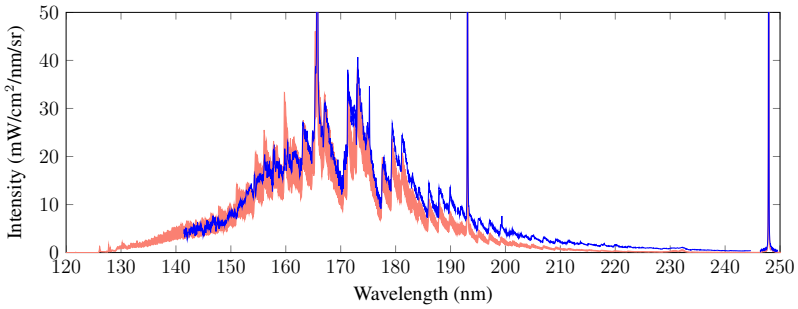

(d) Experiment (blue) and SPECAIR calculations (red) using DeLeon electronic transition moment function with a 0.5 cm absorption path length of cold CO_2 ($x_{CO2} = 0.078$).

Figure 13

Experiment = 606	
Chantranupong	819 ± 153
Cheng	502 ± 94
DeLeon	447 ± 83
Kirby	632 ± 117

Table 1: Integrals of the measured/theoretical spectra between 165 and 220 nm in $mW/cm^2/sr$. The theoretical spectra used for the calculation correspond to those in Figs. 13a-13d and include CO_2 absorption. However, the impact of this absorption is minimal given the wavelength bounds of the integral. The uncertainty bounds on the SPECAIR calculations correspond to the minimum and maximum values based upon the uncertainty in the temperature measurement. The uncertainty for the experimental value is estimated to be primarily from the reported uncertainty of the calibration source ($\pm 5\%$, [35]). The total uncertainty for the experimental value is estimated at $\pm 6\%$ or $\pm\, 36\, mW/cm^2/sr$.

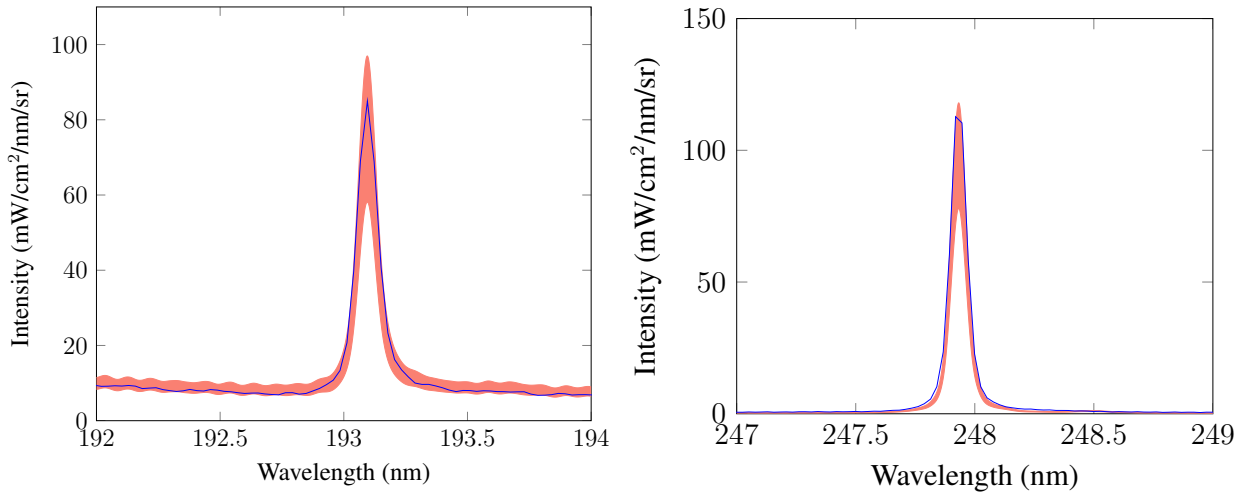

Figure 14: Zoom on the 193 nm C feature (left) and 248 nm C feature (right). Experiment is blue and SPECAIR calculation is in red. For reference, the SPECAIR calculation shown here used the Kirby ETMF for the underlying CO(4+) emission. The apparent shift in the location of the carbon 193 feature relative to the SPECAIR calculation is believed to be an artifact of the wavelength calibration rather than a real shift in the feature.

5. Conclusion

This paper presents VUV experimental data of CO(4+) emission and assesses the performance of radiation transition probabilities obtained from various ETMFs available in the literature. A McPherson VUV spectrometer was used to spectrally analyze the emission coming from an atmospheric pressure plasma torch facility. To avoid oxygen absorption from the surrounding air, a specially designed system was put in place to make measurements down to 140 nm.

The temperature of the plasma was measured using atomic emission lines. These temperature measurements were used to predict the C_2 Swan emission and found to be consistent with measured emission spectra, suggesting the plasma to be in chemical and thermal equilibrium. The Swan band was also shown to be reproduced with the VUV spectrometer, indicating that the vacuum system attachments, with its cooling and argon purge, did not significantly alter the plasma properties.

At lower wavelengths (< 165 nm), absorption from cold gas (likely some combination of CO_2 and O_2) causes the signal to drop off. At these lower wavelengths, the spectra are also heavily

optically thick and thus the calculations are insensitive to the ETMF employed. We find that the ETMFs of Kirby and Cooper or Spielfiedel predict the measured emission coming from the CO(4+) bands between 162-210 nm. The other ETMF's examined in this paper could be said to plausibly match the data over some narrower range centered around 160 nm, but deviate beyond the error bounds at higher wavelengths. One notable exception is the ETMF of Chatranupong, which comes into agreement with the measured data above 220 nm, while the Kirby ETMF over-predicts emission in this range. Based on the relationship of the r-centroid to wavelength (Figure 2), this suggests that the ETMF of Chatranupong may be more accurate for larger separations (>2.7 Bohr) than that of Kirby. Presently, however, SPECAIR retains the transition moments obtained from the ETMF of Kirby - see Appendix C for the conventions used in the calculation of these transition moments. The spectroscopic data based on the ETMF of Kirby, as well as the measured temperature profile and CO(4+) spectrum, are available for download and linked to this article on the journal website.

Acknowledgments

We would like to acknowledge the contributions of Carolyn Jacobs, Umar A Sheikh, Richard Morgan and Victor Gondret who participated in the development of this VUV system. The VUV spectrometer was obtained as part of an International NASA Space Act Agreement for Equilibrium radiation measurements. Augustin Tibère-Inglesse was supported by a CIFRE doctoral grant (number 42701092/20160218/JSE) with ArianeGroup (technical monitor: Laurent Visconti).

References

[1] W.C. Pitts and R.M. Wakefield. Performance of entry heat shields on Pioneer Venus probes. *Journal of Geophysical Research*, 85(A13):8333–8337, 1980.

[2] B.A. Cruden, D. Prabhu, and R. Martinez. Absolute radiation measurement in Venus and Mars entry conditions. *Journal of Spacecraft and Rockets*, 49(6):1069–1079, 2012.

[3] D. Bose, J.H. Grinstead, D.W. Bogdanoff, and M.J. Wright. Shock Layer Radiation Measurements and Analysis for Mars Entry. Technical Report AIAA 2019-3006, NASA Ames Research Center, 2009.

[4] J.H. Grinstead, M.J. Wright, D.W. Bogdanoff, and G.A. Allen. Shock radiation measurements for Mars aerocapture radiative heating analysis. *Journal of Thermophysics and Heat Transfer*, 23(2):249–255, 2009.

[5] Christopher Johnston, Aaron Brandis, and Kenneth Sutton. Shock Layer Radiation Modeling and Uncertainty for Mars Entry. In *43rd AIAA Thermophysics Conference*, 2012.

[6] M.K. Lockwood et al. Systems analysis for a Venus aerocapture mission. Technical Report TM-2006-214291, NASA, 2006.

[7] M.K. Lockwood et al. Aerocapture Systems Analysis for a Titan Mission. Technical Report TM-2006-214273, NASA, 2006.

[8] J.L. Hall, M.A. Noca, and R.W. Bailey. Cost-benefit analysis of the aerocapture mission set. *Journal of Spacecraft and Rockets*, 42(2):309–320, 2005.

[9] A.M. Brandis, C.O. Johnston, B.A. Cruden, D.K. Prabhu, A.A. Wray, Y. Liu, D.W. Schwenke, and D. Bose. Validation of CO 4th positive radiation for Mars entry. *Journal of Quantitative Spectroscopy and Radiative Transfer*, 121:91 – 104, 2013.

[10] Aaron Brandis, Christopher Johnston, Marco Panesi, Brett Cruden, Dinesh Prabhu, and Deepak Bose. Investigation of Nonequilibrium Radiation for Mars Entry. In *51st AIAA Aerospace Sciences Meeting including the New Horizons Forum and Aerospace Exposition*, 2013.

[11] Brett A. Cruden, Aaron M. Brandis, and Dinesh K. Prabhu. Compositional Dependence of Radiance in CO_2/N_2/Ar Systems. In *44th AIAA Thermophysics Conference*, 2013.

[12] C.O. Johnston and A.M. Brandis. Modeling of nonequilibrium CO fourth-positive and CN violet emission in CO_2–N_2 gases. *Journal of Quantitative Spectroscopy and Radiative Transfer*, 149:303 – 317, 2014.

[13] R. L. Macdonald, A. Munafò, C. O. Johnston, and M. Panesi. Nonequilibrium radiation and dissociation of CO molecules in shock-heated flows. *Phys. Rev. Fluids*, 1:043401, Aug 2016.

[14] C.O. Johnston, B.R. Hollis, and K. Sutton. Non-Boltzmann modeling for air shock-layer radiation at lunar-return conditions. *Journal of Spacecraft and Rockets*, 45(5):879–890, 2008.

[15] C.O. Johnston, B.R. Hollis, and K. Sutton. Spectrum modeling for air shock-layer radiation at lunar-return conditions. *Journal of Spacecraft and Rockets*, 45(5):865–878, 2008.

[16] Y. Liu, W. Huo, A. Wray, and D. Carbon. Electron Stark broadening database for atomic N, O, and C lines. In *43rd AIAA Thermophysics Conference*, number AIAA 2012-2739, 2012.

[17] Arnold JO Whiting EE, Yen L and Paterson JA. Nonequilibrium and equilibrium radiative transport and spectra program: user manual. Technical Report NASA RP-1389, NASA Ames Research Center, Aerothermodynamics Division, 1996.

[18] R. L. DeLeon. CO (A–X) electric dipole transition moment. *The Journal of Chemical Physics*, 89(1):20–24, 1988.

[19] R. L. DeLeon. Erratum: CO (A–X) electric dipole transition moment [j. chem. phys. 89, 20 (1988)]. *The Journal of Chemical Physics*, 91(9):5859–5860, 1989.

[20] Kate Kirby and David L. Cooper. Theoretical study of low-lying $^1\Sigma^+$ and $^1\Pi$ states of CO. II. Transition dipole moments, oscillator strengths, and radiative lifetimes. *The Journal of Chemical Physics*, 90(9):4895–4902, 1989.

[21] A. Spielfiedel, W. Tchang-Brillet, F. Dayou, and N. Feautrier. *Ab-initio* calculation of the dipole transition moment and band oscillator strengths of the CO (A-X) transition. *Astronomy and Astrophysics*, 346:699–704, 1999.

[22] Lek Chantranupong, K. Bhanuprakash, Michael Honigmann, Gerhard Hirsch, and Robert J. Buenker. A configuration interaction study of the oscillator strengths for various low-lying transitions of the co molecule. *Chemical Physics*, 161(3):351 – 362, 1992.

[23] Junxia Cheng, Hong Zhang, and Xinlu Cheng. Spectral Study of $A^1\Pi$ - $X^1\Sigma^+$ Transitions of CO Relevant to Interstellar Clouds. *The Astrophysical Journal*, 859(1):19, may 2018.

[24] C.O. Laux. *Optical Diagnostics and Radiative Emission of Air Plasmas*. PhD thesis, Stanford University, Dept. of Mechanical Engineering, 1993.

[25] C O Laux, T G Spence, C H Kruger, and R N Zare. Optical diagnostics of atmospheric pressure air plasmas. *Plasma Sources Science and Technology*, 12(2):125, 2003.

[26] SPECAIR, Software Package, Ver. 3.0, SpectralFit S.A.S., `http://www.spectralfit.com`.

[27] R. Farrenq, G. Guelachvili, A.J. Sauval, N. Grevesse, and C.B. Farmer. Improved Dunham coefficients for CO from infrared solar lines of high rotational excitation. *Journal of Molecular Spectroscopy*, 149(2):375 – 390, 1991.

[28] J.D. Simmons, A.M. Bass, and S.G. Tilford. The fourth positive system of carbon monoxide observed in absorption at high resolution in the vacuum ultraviolet region. *Astrophysical Journal*, 155:345–358, 1969.

[29] C.O. Laux and C.H. Kruger. Arrays of radiative transition probabilities for the N_2 first and second positive, NO beta and gamma, N_2^+ first negative, and O_2 Schumann-Runge band systems. *Journal of Quantitative Spectroscopy and Radiative Transfer*, 48(1):9 – 24, 1992.

[30] A. Schadee. Unique definitions for the band strength and the electronic-vibrational dipole moment of diatomic molecular radiative transitions. *Journal of Quantitative Spectroscopy and Radiative Transfer*, 19(4):451 – 453, 1978.

[31] R. W. Field, O. Benoist d'Azy, M. Lavollée, R. Lopez-Delgado, and A. Tramer. Radiative decay rates from deperturbed v=0–7 vibrational levels of CO $A^1\Pi$ measured using synchrotron radiation. *The Journal of Chemical Physics*, 78(6):2838–2846, 1983.

[32] E.E. Whiting, A. Schadee, J.B. Tatum, J.T. Hougen, and R.W. Nicholls. Recommended conventions for defining transition moments and intensity factors in diatomic molecular spectra. *Journal of Molecular Spectroscopy*, 80(2):249 – 256, 1980.

[33] M.E. MacDonald, C.M. Jacobs, C.O. Laux, F. Zander, and R.G. Morgan. Measurements of air plasma/ablator interactions in an inductively coupled plasma torch. *Journal of Thermophysics and Heat Transfer*, 29(1):12–23, 2014.

[34] A.C. Tibère-Inglesse, S.D. McGuire, P. Mariotto, and C.O. Laux. Validation cases for recombining nitrogen and air plasmas. *Plasma Sources Science and Technology*, 27(11):115010, 2018.

[35] J.Z. Klose, J.M. Bridges, and W.R. Ott. Radiometric calibrations of portable sources in the vacuum ultraviolet. *Journal of Research of the National Bureau of Standards*, 93(1):21–39, 1988.

[36] B. J. McBride and S. Gordon. Computer program for calculating and fitting thermodynamic functions. Technical report, NASA RP-1271, 1992.

[37] L. Caillault, J. Andreasson, J. Risberg, and C. Laux. Modeling the spectral radiation of a methane/nitrogen plasma test case 4. *European Space Agency, (Special Publication) ESA SP*, 629, 11 2006.

[38] Pablo J. Bruna and James S. Wright. Theoretical study of the transition probabilities of the doubly-excited states $E^1\Sigma_g^+$ of C_2 and $2^2\Sigma_g^+$ of C_2^+. *The Journal of Physical Chemistry*, 96(4):1630–1640, 02 1992.

[39] B.A. Thompson, P. Harteck, and R.R. Reeves. Ultraviolet absorption coefficients of CO_2, CO, O_2, H_2O, N_2O, NH_3, NO, SO_2, and CH_4 between 1850 and 4000 Å. *Journal of Geophysical Research*, 68(24):6431–6436, 1963.

[40] K.M. Watanabe, M. Zelikoff, and E.C.Y. Inn. Absorption coefficients of several atmospheric gases. Technical Report 53-23, Air Force Cambridge Research Center, 1953.

[41] A. Kramida, Yu. Ralchenko, J. Reader, and NIST ASD Team (2018). NIST Atomic Spectra Database (version 5.6.1).

[42] C.F. Fischer. Some improved transition probabilities for neutral carbon. *Journal of Physics B: Atomic, Molecular and Optical Physics*, 39(9):2159–2167, 2006.

[43] H.R. Griem. *Spectral Line Broadening by Plasmas*. Academic Press, 1974.

[44] H.R. Griem. *Principles of Plasma Spectroscopy*. Cambridge University Press, 1997.

Appendix A.

Figures A.15 and A.16 show CO(4+) spectra calculated in the optically thin limit for a temperature of 6300 K, which corresponds approximately to the centerline temperature of the jet. Figure A.15 identifies the bands coming from various vibrational levels of the *A* electronic state. Note that emission from $v = 0$ is responsible for the central portion of emission centered around 160 nm, whereas the higher vibrational levels emit mostly on the wings. Figure A.16 identifies the main vibrational bands in the range 140-240 nm.

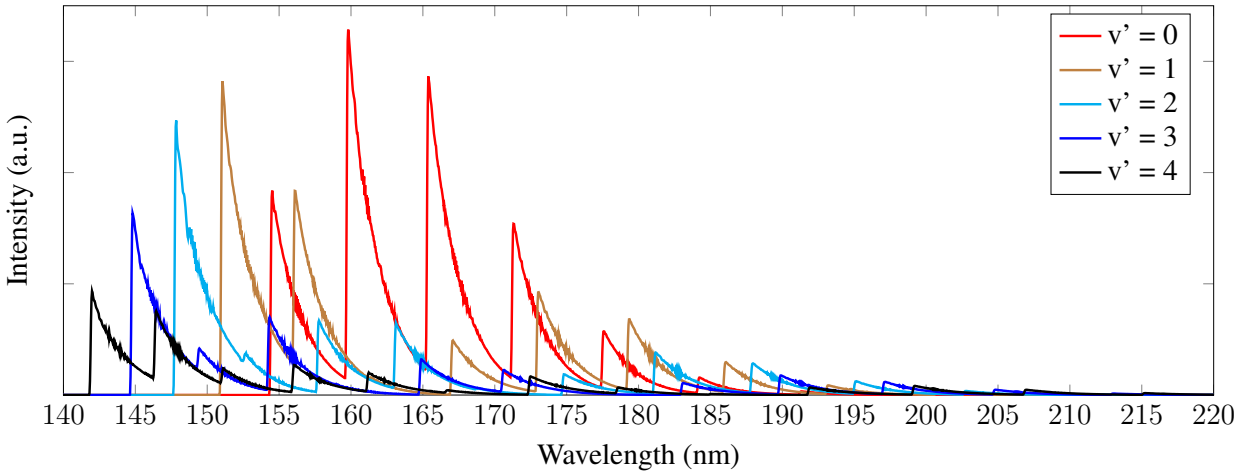

Figure A.15: Spectra emitted by the first five vibrational levels of the electronic *A* state in LTE at 6300 K, 1 atm (optically thin SPECAIR calculations).

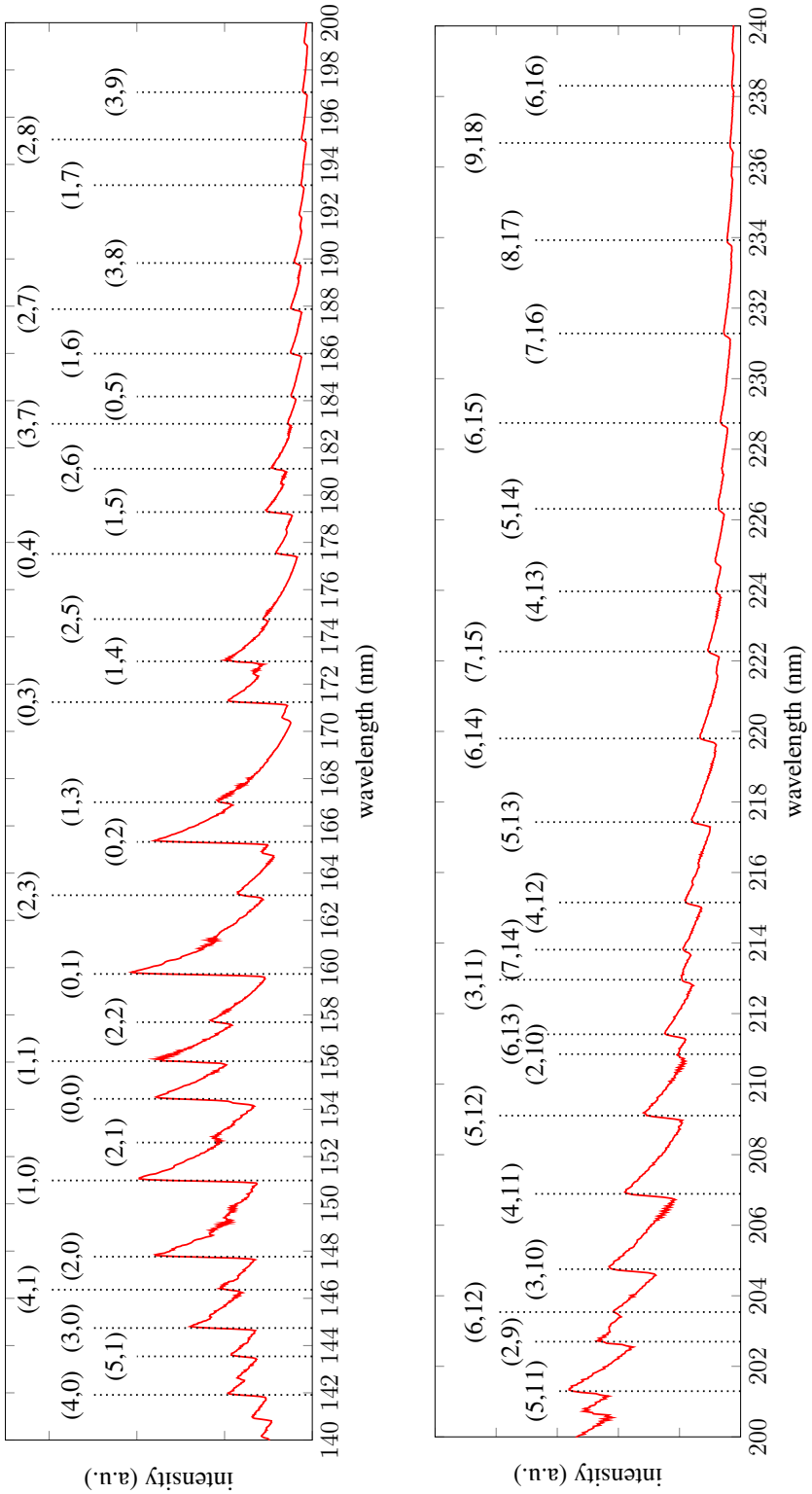

Figure A.16: Vibrational bands (ν', ν'') present in the calculated spectrum.

Appendix B. Line broadening calculations

The majority of the atomic lines measured in the VUV/UV spectrum, as well as a portion of the CO(4+) spectrum, are optically thick to varying degrees. To account for self-absorption along the line-of-sight, it is necessary to take into account the appropriate line broadening mechanisms. These include Doppler, Stark, resonance, van der Waals and natural line broadening. All of these are calculated in SPECAIR. The dominant mechanism is found to be Doppler broadening, which is described by a Gaussian lineshape of full width at half maximum (FWHM) given by:

$$\Delta\lambda_{Doppler} = \lambda_{ul}\sqrt{\frac{8kT\ln 2}{mc^2}} \tag{B.1}$$

For atoms, van der Waals broadening is also found to be important and is estimated based upon the approach detailed by Griem.[43, 44] We use the following formula, adapted from Griem [44], for the Lorentzian FWHM of carbon lines:

$$\Delta\lambda_{vdw} = \sum_p \frac{\lambda^2}{c}\left(\sqrt{\frac{8kT}{\pi}}\right)^{3/5}\left(\frac{\hbar^5\overline{R^2}}{m_e^3}\right)^{2/5}\left(\frac{p}{kT}\right)\left(\frac{X_p}{E_p^{4/5}m_{rp}^{3/10}}\right) \tag{B.2}$$

where all values are in SI units. m_e is the mass of the electron, X_p the mole fraction of the perturber, E_p the energy of the excited state of the perturber connected to its ground state by an allowed transition and m_{rp} the reduced mass of the radiator and the perturber. The formula for the parameter R is taken from Griem:

$$\overline{R^2} = \frac{1}{2}\frac{E_H}{E_\infty - E_i}\left[5\frac{E_H}{E_\infty - E_i} + 1 - 3l_i(l_i+1)\right] \tag{B.3}$$

where E_H is the ionization energy of the hydrogen atom, E_∞ is the ionization energy of the radiating atom and E_i is the excited state energy of the radiator. l_i is the orbital angular momentum quantum number of the radiating state. We increased the FWHM calculated by Eqn. B.2 by a multiplicative factor of $n_e^{2/5}$, where n_e is the number of valence electrons of the perturber. This is done based upon a remark by Griem in section 4.8 of his text.[44]

Table B.2 shows the parameters used in Eqn. B.3 for the van der Waals calculation. Argon is the perturber present in the highest quantities ($X_p \sim 0.84$) and, for this perturber, we used $E_p = 11.6\,eV$, $m_{rp} = 9.2\,amu$ and $n_e = 6$. Table B.3 shows the Doppler and van der Waals FWHMs calculated with the equations above for the conditions at the center of the plasma jet (T = 6300 K, p = 1 atm). These are used for the SPECAIR calculation of the carbon lines at 193 and 248 nm.

Table B.2: Parameters used in Eqn. B.3 for the line broadening calculation for the 193 and 248 nm carbon lines.

$E_H\,(eV)$	$E_\infty\,(eV)$	$E_i\,(eV)$	l_i
13.6	11.3	7.68	0

Table B.3: Dominant broadening linewidths for two of the atomic carbon lines in the VUV.

	Doppler (FWHM, pm)	van der Waals (FWHM, pm)
C I (193 nm)	3.17	0.38
C I (248 nm)	4.07	0.63

Appendix C.

The spectroscopic data for the CO(4+) transition based on the ETMF of Kirby (Ref. [20]) are available for download as an Excel file on the journal website. This data was found to yield the best agreement with experimental data as shown in Fig. 12a and are now used in the SPECAIR radiation code. The conventions outlined in Refs. [30, 24] were used. These lead to a set of equations linking the square of the electronic-vibrational transition moment $(R_e^{\nu',\nu''})^2$ to the values reported in Table C.1. These are as follows:

$$\begin{aligned}
A_{\nu',\nu''} &= \frac{64\pi^4\nu^3\left(2-\delta_{0,\Lambda'+\Lambda''}\right)}{3hc^3\left(2-\delta_{0,\Lambda'}\right)}(R_e^{\nu',\nu''})^2 = \left(2.026\times10^{-6}\right)\left(\overline{\nu}_{\nu',\nu''}\right)^3\frac{2-\delta_{0,\Lambda'+\Lambda''}}{2-\delta_{0,\Lambda'}}(R_e^{\nu',\nu''})^2 \\
f^{abs}_{\nu',\nu''} &= \frac{8\pi^2 m_e\nu\left(2-\delta_{0,\Lambda'+\Lambda''}\right)}{3he^2\left(2-\delta_{0,\Lambda''}\right)}(R_e^{\nu',\nu''})^2 = \left(3.0376\times10^{-6}\right)\overline{\nu}_{\nu',\nu''}\frac{2-\delta_{0,\Lambda'+\Lambda''}}{2-\delta_{0,\Lambda''}}(R_e^{\nu',\nu''})^2 \\
f^{emis}_{\nu',\nu''} &= \frac{2-\delta_{0,\Lambda''}}{2-\delta_{0,\Lambda'}}f^{abs}_{\nu',\nu''} \\
\sum(R_e^{\nu',\nu''})^2 &= \left(2-\delta_{0,\Lambda'+\Lambda''}\right)(2S+1)\,(R_e^{\nu',\nu''})^2
\end{aligned} \tag{C.1}$$

where $\sum(R_e^{\nu',\nu''})^2$ represents the sum of the electronic-vibrational transition moment across all electronic subtransitions. In the above expressions, $\overline{\nu}_{\nu',\nu''}$ is the wavenumber of the transition in cm^{-1} and $R_e^{\nu',\nu''}$ is in atomic units (ea_0, where a_0 is the Bohr radius). Λ' and Λ'' are the projected orbital angular momentum quantum numbers of the upper and lower states respectively. $\delta_{i,j}$ represents the Kronecker delta function.